Seismic array measurements at Virgo's West End Building for the configuration of a Newtonian-noise cancellation system

Maria C. Tringali, Tomasz Bulik

Astronomical Observatory Warsaw University, 00-478 Warsaw, Poland

Jan Harms

Gran Sasso Science Institute (GSSI), I-67100 LAquila, Italy
INFN, Laboratori Nazionali del Gran Sasso, I-67100 Assergi, Italy

Irene Fiori

European Gravitational Observatory (EGO), I-56021 Cascina, Pisa, Italy

Federico Paoletti

INFN, Sezione di Pisa, I-56127 Pisa, Italy

Neha Singh, Bartosz Idzkowski, Adam Kutynia, Krzysztof Nikliborc, Maciej Suchiski

Astronomical Observatory Warsaw University, 00-478 Warsaw, Poland

Alessandro Bertolini, Soumen Koley

Nikhef, Science Park, 1098 XG Amsterdam, Netherlands

Abstract. Terrestrial gravity fluctuations produce so-called Newtonian noise in interferometric gravitational-wave detectors, which is one of the primary noise sources at low frequencies. In this paper, we present a detailed characterization of the seismic field at Virgo's West End Building as part of the development of a Newtonian-noise cancellation system. The cancellation system will use optimally filtered data from a seismometer array to produce an estimate of the Newtonian noise generated by the seismic field, and to subtract this estimate from the gravitational-wave data. Using data from an array of 38 sensors, we show that seismic correlations are complicated due to Virgo's infrastructure, but Wiener filtering applied to seismic data can still be very efficient. With the division of the building's foundation into separated platforms/concrete slabs, and with properties of the seismic field varying across the different parts, we conclude that the arrays to be used for the Newtonian-noise cancellation at Virgo will require a relatively large number of seismometers per test mass, i.e., significantly more than 10, and that the Wiener filter needs to be updated regularly, probably more often than every hour, to achieve stationarity of the noise residuals.

1. Introduction

Terrestrial gravity fluctuations, known as Newtonian noise (NN), were first predicted to be a limiting noise source for ground-based gravitational-wave (GW) detectors by Weiss [1], and first analyzed in greater detail by Saulson [2]. The sources of NN can be classified in two main components: seismic and atmospheric density fluctuations.

Atmospheric NN is produced by pressure fluctuations, and advection of temperature and humidity fields. An acoustic observation campaign performed at the Virgo site [3] highlights the relevance to take into account a reduction of the acoustic noise in the buildings for future upgrades of Advanced Virgo (AdV), and in case of underground detectors, where acoustic NN is strongly reduced, the contribution coming from the cavities housing the test masses is close to the targeted sensitivity at a few Hz.

The main types of seismic waves relevant to NN are compressional waves, shear waves, and Rayleigh waves [4]. Compressional and shear waves are known as P-waves and S-waves, respectively. P-waves arrive first right after an earthquake while S-waves follow them, hence the name primary (P) and secondary (S). Compressional waves are longitudinal waves producing displacement along the direction of propagation. The nature of shear waves is transversal generating displacement perpendicular to the direction of propagation. Both wave types, compressional and shear, are body waves since they can propagate through media in all directions. Rayleigh waves travel along the surface of media producing elliptical motion of the ground particles. The wave amplitude decreases exponentially as distance from the surface increases. Seismic NN is produced by compression of the ground medium or by surface and interface displacement.

At low frequencies, below 20 Hz, NN affects the sensitivity of the Advanced LIGO [5] and Virgo [6] detectors and turns out to be the limiting noise source for future detector sensitivity in this frequency range [4, 7, 8, 9]. As reported in [9, 10, 11, 12], the first approach to mitigate this kind of noise is obtained by means of a Wiener filter. It is calculated from correlations between data of environmental sensors and data observed at the target channel (detector output) where the noise has to be reduced. In this work, we perform an investigation and characterization of the seismic field measured by an array of seismometers deployed at the West End building (WEB) of the Virgo interferometer in February 2018. We use the measurements of the seismic field to investigate the quality of the Wiener filtering method. In particular, we investigate the optimal number of sensors, optimal sensor array, and stability of the method with time.

The paper is organized as follows. In Section 2, we introduce the Wiener filter for single-input single-output and multi-input single-output noise cancellation. In Section 3, we give a brief description of the seismometer array setup. Section 4 collects the main results of Wiener filtering study. Finally, in section 5, we report the conclusion of this work.

2. Wiener filtering theory

In this section, we summarize the equations that determine a Wiener filter in frequency domain. We consider two implementations: the single-input single-output, and the multi-input single-output filter. The latter is of interest for the purpose of this work. The argumentation of this topic is based on [13][14].

2.1. Single-input Single-Output (SISO) filter

In general, Wiener filters are used to reduce the variance of data in a target channel exploiting correlations with auxiliary channels. They are linear filters, which means that they are applied as simple convolutions in time domain. Let $X(f)$ be the target and $S(f)$ the input signal of the filter from a single auxiliary channel in frequency domain. Since a convolution in time domain is described by a simple multiplication of Fourier amplitudes in frequency domain, the filter output, $\hat{X}(f)$, is given by:

$$\hat{X}(f) = W(f)S(f) , \tag{1}$$

where $W(f)$ is filter response in frequency domain. The Wiener filter is the optimal linear filter in the sense of minimizing mean-squared error signal $E[e(f)^2]$ if all data are stationary. The estimation error is given by

$$e(f) = X(f) - \hat{X}(f) = X(f) - W(f)S(f) , \tag{2}$$

and the mean-square estimation error at a frequency f can then be written

$$E\big[|e(f)|^2\big] = E\big\{[X(f) - W(f)S(f)]^*[X(f) - W(f)S(f)]\big\} \tag{3}$$

$$= E\big[|X(f)|^2 - 2\Re(X(f)^*W(f)S(f)) + |W(f)S(f)|^2\big] \tag{4}$$

$$= E\big[|X(f)|^2\big] - 2\Re(W(f)E\big[X(f)^*S(f)\big]) + E\big[|W(f)S(f)|^2\big] \tag{5}$$

where $E[\cdot]$ is the expectation value and symbol $*$ denotes the complex conjugate. The filter producing the least mean-square error is obtained by setting to zero the derivative of this last equation with respect to the filter $W(f)$:

$$\frac{\partial}{\partial W(f)}E\big[|e(f)|^2\big] = 0 \qquad \longrightarrow \qquad W(f) = P_{SS}(f)^{-1}P_{XS}(f) , \tag{6}$$

where $P_{SS}(f) = E[|S(f)|^2]$ is the power spectrum of the input signal $S(f)$ and $P_{XS}(f) = E[X(f)S^*(f)]$ is the cross-power spectrum between input and target signal $X(f)$.

2.2. Multiple-input Single-output (MISO) filter

In this section, we briefly describe the case of a multiple-input single-output (MISO) filter. Formally, the equations are identical to the equations of the last section, just that we now need to introduce vectors and matrices of cross-power spectra.

We suppose to have a system with M input signals and a single output. Similarly to the SISO filter, the input-output relation becomes

$$\hat{\vec{X}}(f) = \vec{W}(f)^T \cdot \vec{S}(f), \tag{7}$$

and the MISO Wiener filter equation is

$$\vec{W}(f) = \mathbf{P}_{SS}(f)^{-1} \cdot \vec{P}_{XS}(f), \tag{8}$$

where $\mathbf{P}_{SS}(f) = E[\vec{S}(f)\vec{S}^\dagger(f)]$ is the $M \times M$ matrix of cross spectra between the M input signals ($\dagger$ denotes the complex-conjugate transposition), and $\vec{P}_{XS}(f) = E[X(f)\vec{S}^*(f)]$ is an M-component vector of cross spectra between the M input signals and the target signal.

3. West End Building seismometer setup

The Virgo detector is an L-shaped laser interferometer that responds to distance changes between suspended test masses caused by passing gravitational waves. Each arm of the interferometer has two test masses separated by about 3 km. Two end buildings, the North and West End Buildings (NEB, WEB), identical in construction and layout, host the two end test masses of the interferometer, while the central building (CEB) hosts the two inner test masses. All of the main optical system and the main part of the seismic isolation system are located inside vacuum tubes and chambers.

The foundation of the WEB (and NEB) consists of two concrete slabs, building platform and tower platform (see left plot of Figure 1). The tower platform carries all of the test-mass suspension and isolation system integrated in the so-called superattenuator [6]. Since the Virgo detector was constructed on soft soil, the slabs need to be supported by poles of several tens of meter length to connect the construction to a deeper, harder layer of the ground. The main reason why the foundation is separated into two slabs is reduction of cost since the requirement of how much the tower platform can sink per year is much stricter than for the rest of the building. Accordingly, the single concrete shell of outer slab is supported by the 30 m deep poles while the tower floor together with clean basement, are supported by a longer set of poles, reaching a more stable gravel layer, 52 m deep at the west arm. Since building and tower platforms are disconnected by a gap of about 1 cm (and less), the construction also provides suppression of seismic noise on the tower platform above 10 Hz as will be shown later. Over time, a step of, now, almost 9 cm has formed due to subsidence between building and tower platform as shown in the right plot of Figure 1.
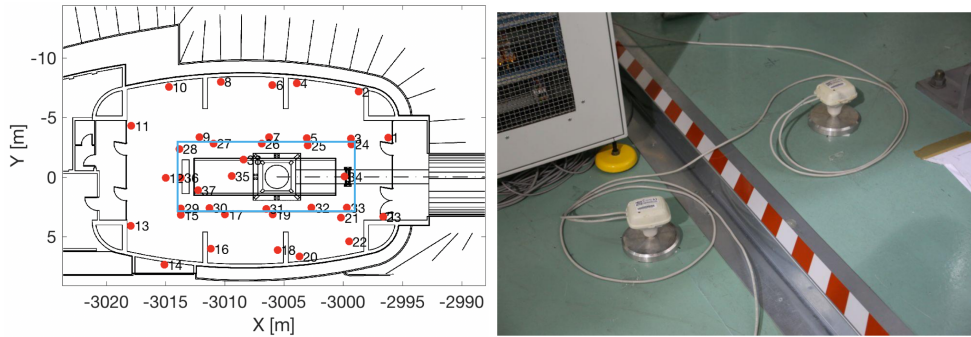

Figure 1. (Left plot) A map of the seismometer positions at West end building at Virgo site. Light blue rectangular perimeter denotes the extent of the tower platform. (Right plot) Two sensors located near (left) and on tower (right) platform, respectively.

The tower platform or inner slab constructed in the central part of the building floor is 6 m wide and 15 m long. It supports the vacuum tank (the so-called *tower*) and the clean room (20 m^2) used for payload installation. The middle of the tower floor on ground level is covered by a thin metal sheet that can be removed to allow the payload insertion. The building platform or outer slab supports the building's structure i.e. the walls and roof. The height of the building is 17 m and the covered area is 17 m wide and 25 m long in the arm direction. The back of each building (towards

negative X values in Figure 1) hosts a technical room with various electro-mechanical infrastructure devices like the $15\,\mathrm{kV}$ power supply, transformers, uninterrupted power supplies, a diesel generator and chilled/hot water generators for air conditioning [15]. The technical room contains some of the major sources of seismic disturbances in the NN band at Virgo.

On January 18 and 19, 2018, an array of 38 seismometers was deployed inside the WEB and another one of 9 seismometers was installed outdoor [16]. Figure 1 shows the positions of indoor sensors: 14 are located near the walls of the WE tower, 9 near the tower platform, 13 on the tower platform and 2 at the sub-surface level of the tower platform. The sensors were manufactured by InnoSeis [17]. They are based on $4.5\,\mathrm{Hz}$ geophones monitoring vertical ground displacement. The housing of the InnoSeis sensors also contains a pre-amplifier and an analog-to-digital converter to avoid issues with excess electromagnetic (EM) noise in analog signal transmissions through several meter long cables in an EM noisy environment.

The indoor sensors were placed on the floor fixing their heavy mount plate with double-sided adhesive tape for a good connection to ground (see the right plot of Figure 1). Outdoor sensors were partially dug into the ground to protect them from the wind. The data acquisition covers 13 days, from January 25 to February 6, 2018 [18]. A central data-acquisition unit used for the readout of the entire array also had the purpose of synchronizing and powering the sensors. The outside sensors operated autonomously. Each of them was independently synchronized using a built-in GPS antenna. The sampling frequency was $500\,\mathrm{Hz}$ for indoor sensors and $250\,\mathrm{Hz}$ for outdoor sensors.
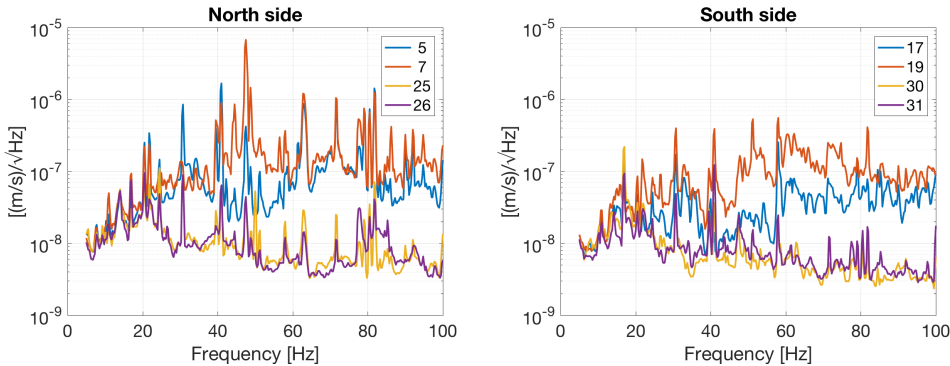

Figure 2. Root of power spectrum densities of two couples of seismometers positioned at North side and other two at South side of West end building, respectively. Sensors 5, 7, 17, 19 (blue and red curves) lies on building platform while sensors 25, 26 30, 31 (yellow and violet curves) on tower platform.

In Figure 2, we report the square-root of power spectral densities (PSDs) of four seismometers positioned on North and South sides of the building. The seismometers were chosen as pairs: one sensor is located on the building platform and the other one on the tower platform with a distance of less than $0.5\,\mathrm{m}$ between them. For frequency values above $\sim 15\,\mathrm{Hz}$, a significant difference in PSDs is evident comparing tower platform (yellow and violet curves) and building platform (red and blue curves).

The explanation for this difference in PSDs is that dominant seismic sources are located outside the tower platform, and the seismic waves that they produce are

sufficiently short above 15 Hz to be reflected from the gap between building and tower platform, i.e., the gap does not reach deep enough into the soil to efficiently reflect seismic waves below 15 Hz. This effect can be characterized in detail by calculating the transfer function between such a pair of seismometers, as shown in Figure 3. One can see that the gap significantly influences correlations between seismometers starting at about 9 Hz.
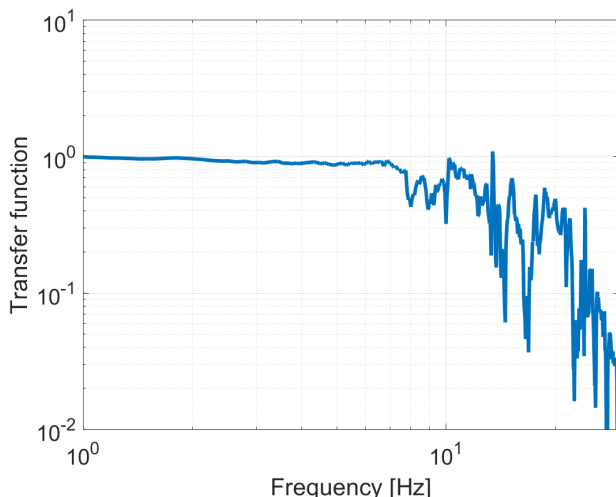

Figure 3. Transfer function (its absolute value) from seismometer on building floor to seismometer on tower platform. The distance between the two seismometers is less than 0.5 m.

4. Wiener filtering investigation

In this section of the paper, we present first results of a Wiener-filtering study. We consider, as case studies, the first hour (UTC) of February 4 and 5, 2018, and we focus on the 1 – 50 Hz frequency band.

4.1. Virgo WEB seismometer array

We first present a characterization of the seismic field in the WEB. In Figure 4, we report seismic spectra of a few selected seismometers located at the wall of the building (4), near the technical room (13), near the tower platform (9), on the building floor (25 and 29), and on the metal sheet (35). The calculation of power spectral densities covers one hour starting from midnight (local time). The data from seismometer 35 clearly stands out above the level of all other units. This is due to the fact that it was positioned on the metal sheet on the tower platform, which vibrates much more strongly than ground probably due to acoustic perturbation. The seismic spectra lie approximately between $10^{-8} \, \mathrm{m\,s^{-1}Hz^{-1/2}}$ and $10^{-7} \, \mathrm{m\,s^{-1}Hz^{-1/2}}$. There are several lines in the spectra that affect the entire building. In particular one can see vibrations at approximately 17 Hz, 21 Hz, 22 Hz, 24 Hz, 31 Hz, 39 Hz ad 41 Hz. The lines are persistent, and some were identified with disturbances from vacuum pumps and cooling fans.
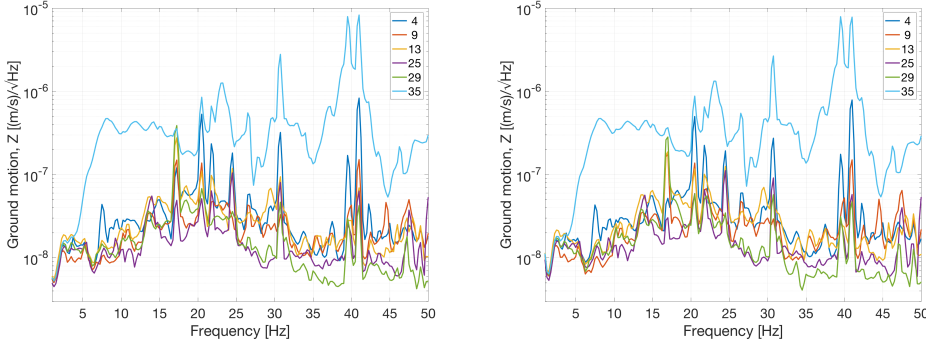
Figure 4. Amplitude spectral densities of WEB seismometer array. The spectra are computed on one hour for February 4th (left plot) and 5th (right plot).

In the analysis presented below, we have down-sampled the data to 250 Hz, and then divided it into 4 s (1000 samples) segments. In the calculation of the spectra, we have used the Hamming window with 50% overlap, and averaged the spectral and cross spectral densities over the full hour.

The array maps in Figure 5 give an overview of the contribution to noise levels at frequency values 10 Hz, 15 Hz and 20 Hz. For some sensors, there can be significant differences between the spectra measured at the two days, but variations are generally small. Especially at 10 Hz, one can see for both days that seismic spectra are stronger towards negative X values, which is consistent with seismic sources being located in the technical room. Focusing on sensors with $X > -3015$ m, there is only a minor difference in spectra between sensors located on the building and tower platform (except for two sensors located close to the north wall). Looking at higher frequencies, the behavior is different. At 15 Hz, in addition to the disturbance by the technical room, major disturbances seem to originate from near the building walls and the vibrations propagate towards the tower platform. The origin of this noise is unclear, and even correlation measurements as shown below do not help to identify the source(s). At 20 Hz, there is a significant difference between spectra among the two slabs of the building. The sources of dominant ground vibrations seem to come from building walls.

Another analysis is the measurement of coherence $\gamma(f)$ between all seismometers in the array. In general, the coherence between two signals $x(t)$ and $y(t)$ is defined as:

$$\gamma(f) = \frac{S_{xy}(f)}{\sqrt{S_x(f) \cdot S_y(f)}}, \tag{9}$$

where $S_{xy}(f)$ is the cross-spectral density between x and y, $S_x(f)$ and $S_y(f)$ the power-spectral densities of x and y. The coherence is a complex-valued function. It plays a crucial role for a deeper understanding of the seismic field, for an accurate estimation of NN, and also for the design of a NN cancellation system [7, 10, 19, 20]. Sensor correlations define the Wiener filter (see Eq.(8)). In Figure 6 we present the real part of coherence $\gamma(f)$ as a function of the relative position of seismometer pairs at three frequencies: 10, 15 and 20 Hz. If the ground were homogeneous and isotropic, and Rayleigh waves dominated, we would expect that coherence evolves smoothly
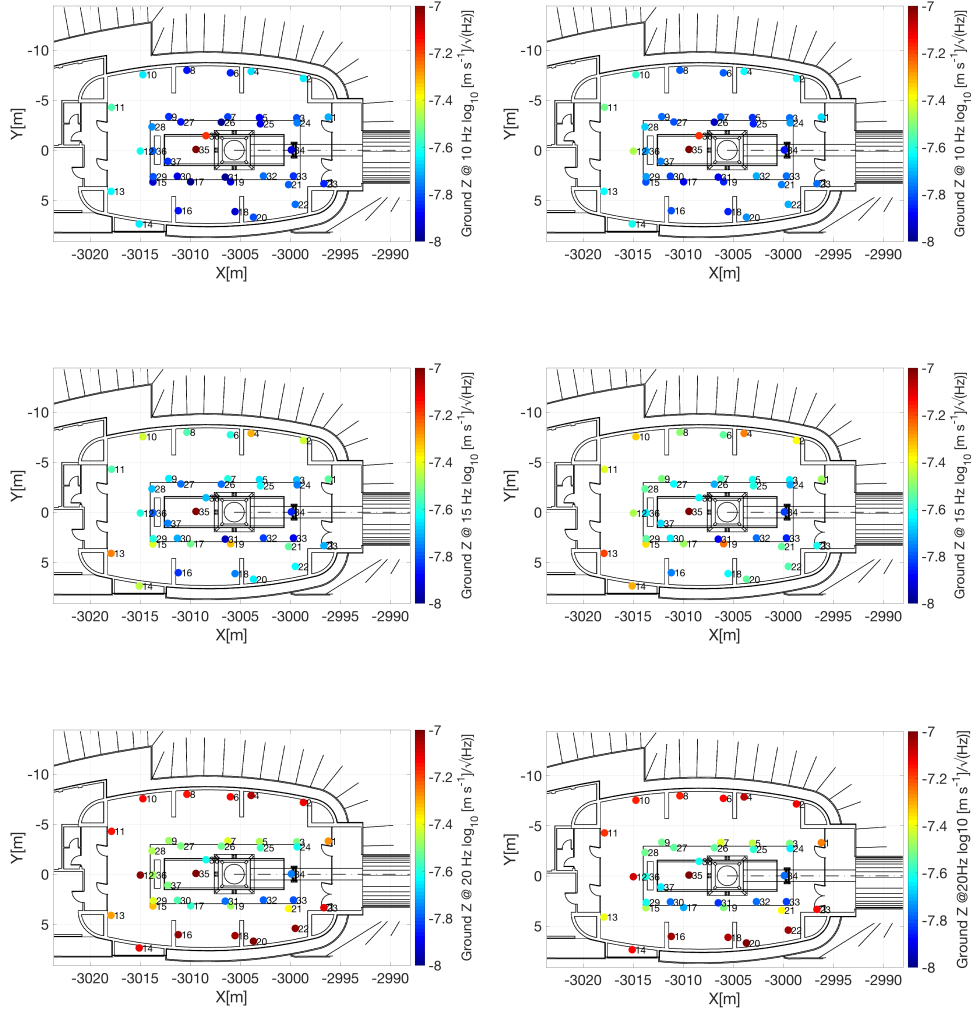
Figure 5. Ground-vibration spectra at sensor locations. Both columns refer to hour 00:00:00 (UTC) of February 4 (left column) and February 5 (right column). The three rows correspond to the frequencies 10, 15, 20 Hz. We present the color coded values of the logarithm of the seismic spectra at each location.

following a Bessel function [8]:

$$\gamma(f) = J_0(2\pi f r/c), \tag{10}$$

where r is the distance between sensors, and c the speed of Rayleigh waves. It is real-valued, because the underlying model of the seismic field is isotropic. However, seismic correlations at the WEB are different: in Figure 6, points of noticeably different color can be next to each other (heterogeneity) and the correlation maps do not have polar symmetry (anisotropy).

Still, at 10 Hz, one can at least discern the underlying Bessel function, since

(a) Data 2018:02:04 h 00:00:00 (UTC)

(b) Data 2018:02:05 h 00:00:00 (UTC)
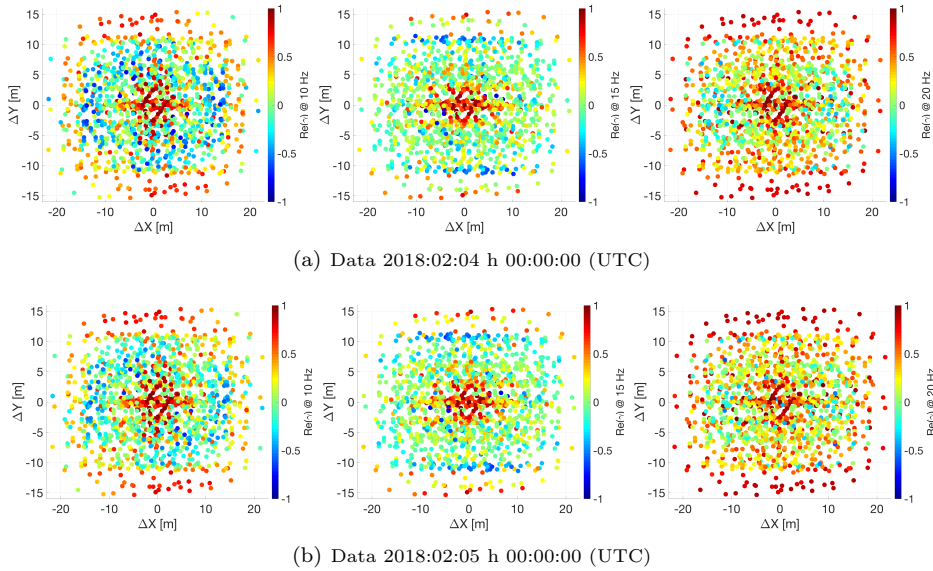
Figure 6. Real part of $\gamma(f)$ between all seismometers at 10, 15 and 20 Hz. The coordinates x,y are relative position vector between two seismometers.

seismic scattering from the tower platform is weak, and seismic sources sufficiently far from all sensors. At 15 Hz, the correlation map assumes an X, Y anisotropy supported by most sensor pairs, while the 20 Hz map appears as an almost random pattern with high values of $\Re(\gamma)$ at almost any distance between seismometers. It is especially intriguing that ground vibrations at the north and south walls have high values of $\Re(\gamma)$, since Figure 5 suggests that there are *local* seismic sources near the walls leading to increased ground motion. We do not have a good explanation to offer. Potential explanations are: (1) sound waves inside the building push coherently on the north and south walls, (2) the increased ground vibration at the walls is not due to local sources, but due to some amplification of ground vibrations caused, for example, by a coupling between ground and walls. Both explanations certainly have their weaknesses, and a dedicated analysis needs to clarify this issue.
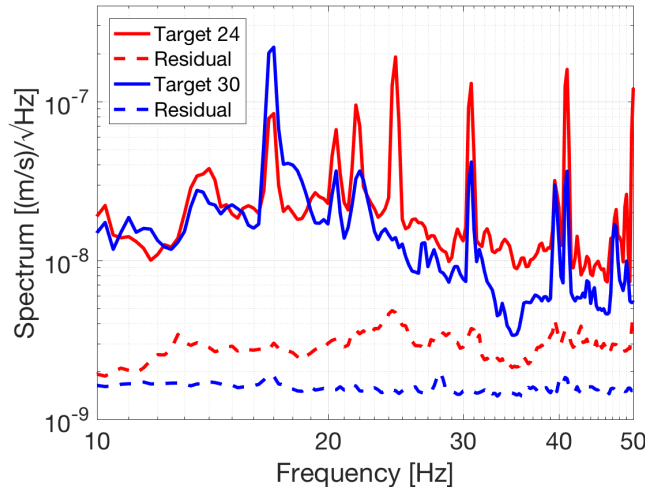
4.2. Wiener filtering

In the context of NN cancellation, the goal of Wiener filtering is to make an estimate of NN using data from a seismic array, and to subtract this estimate from the GW data. Since the NN lies still below the GW noise floor, we will test the potential quality of the Wiener filtering by trying to reconstruct the signal from a target seismometer using the remaining seismometers as inputs to the Wiener filter. We address two issues. First, we estimate the quality of the Wiener filtering as a function of the number of seismometers used as filter input. We also investigate the optimal choice of seismometers, that is the optimum array layout. Second, given a layout, we verify the stability of the Wiener filter with time by analyzing the stability of subtraction performance over a few hours.

The residual signal remaining after the subtraction of the Wiener filter output

from the known target signal provides an estimate of the efficiency of Wiener filtering method. The average of this residual relative to the original NN spectrum can be written as:

$$R(f) = 1 - \frac{\vec{C}_{ST}^T(f) \cdot \mathbf{C}_{SS}^{-1}(f) \cdot \vec{C}_{ST}(f)}{C_{TT}(f)}, \tag{11}$$

where C_{ST} denotes the vector of cross-spectral densities between the target sensor and seismometers, $\mathbf{C}_{SS}$ represents the matrix of cross-spectral densities between all seismometers in the array, and C_{TT} is the power spectral density of the target sensor. In the plots and analysis below, we will show the square root of the residual R to refer to the noise affecting signal amplitudes instead of power.

Figure 7. Vertical ground motion at sensors 24 and 30, and corresponding residuals after Wiener filtering with all other seismometers of the array used as input channels.
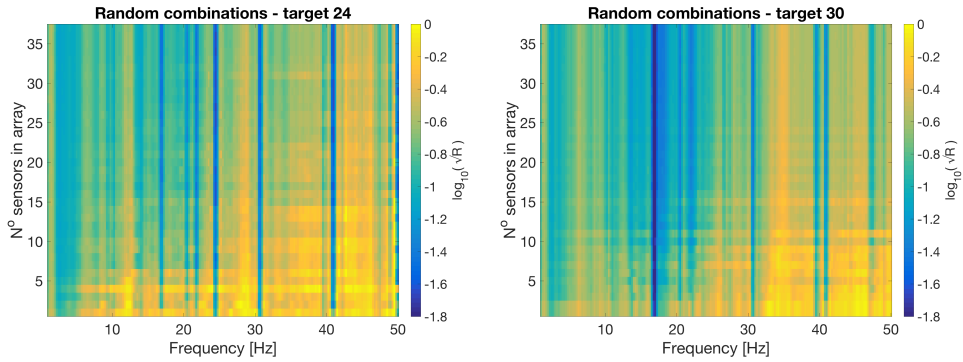
Figure 8. Residuals for well-performing array configurations minimizing Eq.(11) at 15 Hz among 10 random selections of seismometers for each value of N. The residuals are computed for February 5, 00:00:00 (UTC) and for two different target sensors.

In order to assess the quality of Wiener filtering as a function of the number and layout of the sensors, we choose to investigate two cases: with target sensor #24 and #30, both located on the tower platform. First, one can compare the spectra of the two target sensors and the residual noise after cancellation with all other seismometers of the array used as input channel as shown in Figure 7. It can be seen that the residual spectra are relatively flat compared to the original spectra. The residual of target 30 is about a factor 10 above the instrument self-noise.

For each number of seismometers picked from the total array as input channels, we select ten random combinations covering the full possible range of $N = 1, \ldots, 37$ of input channels. Among, these random combinations, we chose the array with best subtraction at 15 Hz. We present the results of the analysis in Figure 8. The plot shows the relative residuals $\sqrt{R}$ as function of the frequency for the best-performing arrays with the given number of sensors. The residuals are computed using the data from February 5 at midnight. The first thing to notice, consistent with Figure 7, is that the noise suppression factor is highest where the original seismic spectra are strongest since the residual spectra are approximately flat. This means that the array captures all the necessary information about the seismic field; below 25 Hz if more than about 6 sensors are used, above 25 Hz if more than about 25 sensors are used. Also, the difference between the two plots in Figure 8 is mostly due to a difference between seismic spectra of sensors 24 and 30, and to a lesser extent a result of limited subtraction performance (again, provided that the number of input channels to the Wiener filter is sufficiently high). For both plots, an outlier is observed in residual values ($\sqrt{R} > 1$). This behaviour can be related to a transient signal in the seismic data and in the light of this, the upper limit of the colobar is set to zero.

It should be noted that for some parts of the graph the filtering seems to worsen with the increase of the reference array. This is due to the fact that we do not investigate all the possible sensor sub-arrays but only generate ten random combinations for each case, and also, picking the best performing array at 15 Hz does not mean that it leads to best performance at other frequencies or that it necessarily improves at other frequencies within increasing sensor number. Thus the results presented in Figure 8 should be considered only as an indication of the Wiener-filtering quality.

| N° of seismometers in sub-array	Target #24	Target #30
1	25	29
2	25, 26	29,31
3	25, 26, 29	27, 29, 31
4	25, 26, 30, 31	26, 27, 29, 31
5	25, 26, 30, 31, 35	24, 25, 27, 29, 31
6	25, 26, 29, 30, 31, 35	24, 25, 27, 29, 31, 33
7	25, 26, 27, 29, 30, 31, 35	24, 25, 26, 29, 31, 33, 35
8	25, 26, 27, 29, 30, 31, 33, 35	24, 25, 26, 27, 29, 31, 33, 35
9	25, 26, 27, 29, 30, 31, 32, 33, 35	24, 25, 26, 27, 29, 31, 32, 33, 35

Table 1. Optimal configurations for target 24 and 30. Sub-arrays are obtained by looping over all possibile configurations.

The second test is to verify how stable the Wiener filtering is over time. To this end, we calculate the Wiener filter using one hour of data starting at midnight and then apply it to the following hours to verify if the residual remains similar. We analyze filter evolution using data from February 5 focusing on the seismometers located on
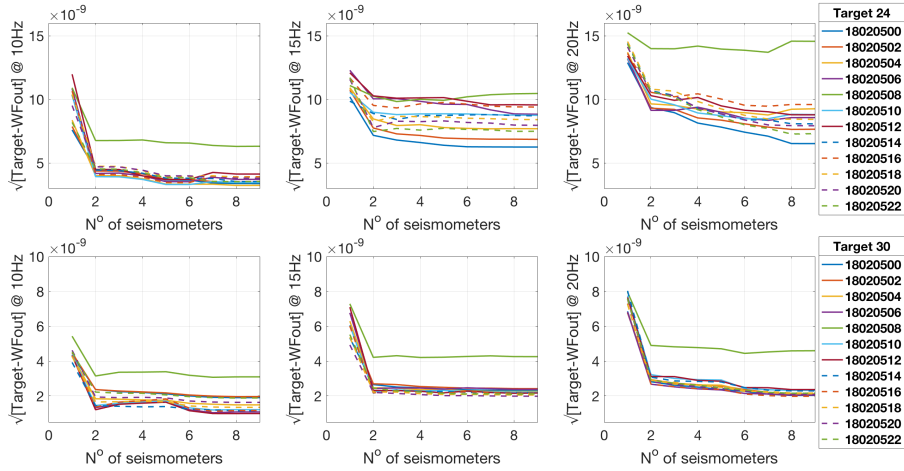
Figure 9. Daily evolution of residuals for well-performing input arrays on tower platform using sensors 24 (top row) and 30 (bottom row) as target channels. The x and y-axes are the number of sensors and the square root of absolute residual, respectively. The Wiener filter is calculated using one hour starting at midnight.

the tower platform. We choose sensors {24 25 26 27 29 30 31 32 33 35} as input sensors, excluding sensors 24 and 30, which serve as the target sensors. Best performing sub-arrays are selected as in the previous study based on the relative residual at 15 Hz. In Figure 9, we present the absolute residual as function of the number of seismometers in the array for several hours during the day of February 5 always using the same Wiener filter calculated at midnight. While there is no trend in the performance to degrade with increasing time, there are significant variations in performance.
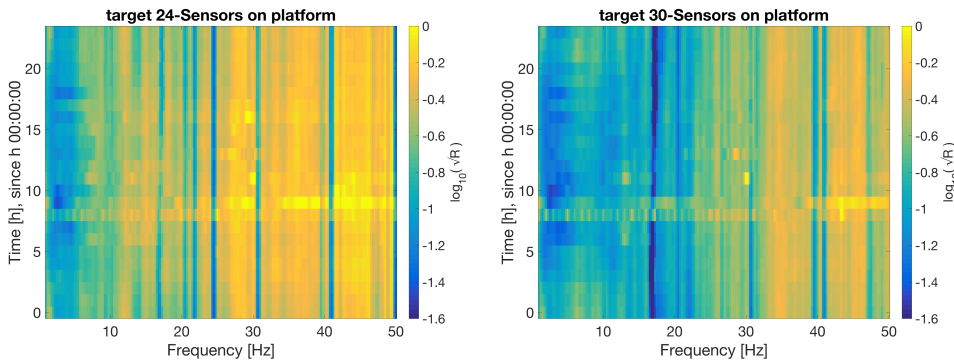
Figure 10. Time frequency map of square root of Wiener filter residuals for nine input sensors located on the tower platform. Data from February 5 is analyzed for target 24 (left plot) and 30 (right plot).

We observe an increased residual (solid green line), corresponding to the hour 08:00:00 (UTC), probably due to strong transients from human activity. However, the behavior of the residuals is different from frequency to frequency. For example,

at 15 Hz and with sensor 24 as target, residual values increase throughout the hours $\sim 7 \cdot 10^{-9}\,\mathrm{ms^{-1}Hz^{-1/2}}$ at midnight to $\sim 1 \cdot 10^{-8}\,\mathrm{ms^{-1}Hz^{-1/2}}$ at 16:00:00 (dashed red line) and then decrease to $\sim 8 \cdot 10^{-9}\,\mathrm{ms^{-1}Hz^{-1/2}}$ at 22:00:00 (dashed green line). The significant variation over time of noise residuals can be attributed to slow diurnal evolution of anthropogenic noise. This means that the Wiener filter will have to be updated at least every hour to guarantee a stable cancellation performance.

We have analyzed in greater detail the case of the array of nine input seismometers on the tower platform. The time-frequency maps were calculated, in which we show the time evolution of Wiener-filter residuals as a function of the frequency. We present the results in Figure 10 for the two target sensors. The residual does not vary significantly over time with the exception of one louder hour at 8am. Overall, the cancellation performance remains stable.

5. Conclusions

In this paper, we presented a characterization of the seismic field at Virgo's West End Building required for the design of a Newtonian-noise cancellation system. Accordingly, the focus lay on spectra and the two-point spatial correlations of the seismic field, and on how these impact the performance of a Wiener filter for the cancellation of seismic signals.

Correlation analyses underlined the presence of inhomogeneities and anisotropies of the seismic field probably generated by local noise sources as well as scattering of the seismic waves from sub-surface structures of the building. These effects become especially visible at higher frequencies, i.e., well above 10 Hz, which is expected if scattering is a cause.

We have performed a case study of Wiener filtering using two different seismometers on the tower platform as target channels. We showed that the subtraction of the target signal can be efficiently achieved with at least six seismometers as input to the Wiener filter at frequencies below 25 Hz, while more seismometers are required at higher frequencies. These numbers are of course only relevant to the cancellation of seismic signals, not Newtonian noise, but it allows us to evaluate the level of correlations between sensors, and we conclude that the extraction of information about the seismic field by the array is exhaustive for the purpose of Newtonian-noise cancellation in the foreseeable future, which means that we will not need more than 38 seismometers for the noise cancellation in the future, and likely, less sensors will be sufficient since the level of degeneracy of array data is very high, i.e., the seismic senors are closer to each other than necessary.

It should be noted though that this only applies to the seismic field especially inside the Virgo building. Ongoing analyses of a new array at Virgo's North End Building, will allow us to assess whether outdoor sensors are required as well, and we cannot, yet, exclude the possibility that there are other significant sources of Newtonian noise such as vibrating vacuum infrastructure in the immediate vicinity of the test masses. The mitigation of noise from these sources would have to be addressed separately.

Another important aspect of Wiener filtering is whether the filter can be implemented as static filter, or whether it needs to be adapted or recalculated regularly. For this purpose, we presented results showing how noise-cancellation performance varies over time when using a static filter. We found a significant variation over time of noise residuals, and these variations can be attributed to slow diurnal evolution

of anthropogenic noise. The results suggest that the Wiener filter will have to be updated at least every hour to guarantee a stable cancellation performance.

Acknowledgments

[1] Rainer Weiss. Electromagnetically coupled broadband gravitational antenna. *MIT Res. Lab. Electron. Q. Prog. Rep*, 105:54–76, 1972.

[2] Peter R. Saulson. Terrestrial gravitational noise on a gravitational wave antenna. *Physical Review D - PHYS REV D*, 30:732–736, 08 1984.

[3] Donatella Fiorucci, Jan Harms, Matteo Barsuglia, Irene Fiori, and Federico Paoletti. Impact of infrasound atmospheric noise on gravity detectors used for astrophysical and geophysical applications. *Phys. Rev. D*, 97:062003, Mar 2018.

[4] Jan Harms. Terrestrial Gravity Fluctuations. *Living Reviews in Relativity*, 18(3), 2015.

[5] The LIGO Scientific Collaboration, J Aasi, B P Abbott, R Abbott, T Abbott, M R Abernathy, K Ackley, C Adams, T Adams, P Addesso, R X Adhikari, V Adya, C Affeldt, N Aggarwal, O D Aguiar, A Ain, P Ajith, A Alemic, et al. Advanced LIGO. *Classical and Quantum Gravity*, 32(7):074001, 2015.

[6] F Acernese, M Agathos, K Agatsuma, D Aisa, N Allemandou, et al. Advanced Virgo: a second-generation interferometric gravitational wave detector. *Classical and Quantum Gravity*, 32(2):024001, 2015.

[7] Jan Harms, Bram J. J. Slagmolen, Rana X. Adhikari, M. Coleman Miller, Matthew Evans, Yanbei Chen, Holger Müller, and Masaki Ando. Low-frequency terrestrial gravitational-wave detectors. *Phys. Rev. D*, 88:122003, Dec 2013.

[8] Jennifer C. Driggers, Jan Harms, and Rana X. Adhikari. Subtraction of Newtonian noise using optimized sensor arrays. *Phys. Rev. D*, 86:102001, Nov 2012.

[9] Jan Harms and Krishna Venkateswara. Newtonian-noise cancellation in large-scale interferometric GW detectors using seismic tiltmeters. *Classical and Quantum Gravity*, 33(23):234001, 2016.

[10] G. Cella. Off-Line Subtraction of Seismic Newtonian Noise. In B. Casciaro, D. Fortunato, M. Francaviglia, and A. Masiello, editors, *Recent Developments in General Relativity*, pages 495–503. Springer Milan, 2000.

[11] M. W. Coughlin, J. Harms, J. Driggers, D. J. McManus, N. Mukund, M. P. Ross, B. J. J. Slagmolen, and K. Venkateswara. Implications of Dedicated Seismometer Measurements on Newtonian-Noise Cancellation for Advanced LIGO. *Phys. Rev. Lett.*, 121:221104, Nov 2018.

[12] M Coughlin, J Harms, N Christensen, V Dergachev, R DeSalvo, S Kandhasamy, and V Mandic. Wiener filtering with a seismic underground array at the Sanford Underground Research Facility. *Classical and Quantum Gravity*, 31(21):215003, 2014.

[13] Jacob Benesty, M Mohan Sondhi, and Yiteng Huang. *Springer handbook of speech processing*. Springer, 2007.

[14] Saeed V Vaseghi. *Advanced digital signal processing and noise reduction*. John Wiley & Sons, 2008.

[15] T. Accadia et al. Virgo: a laser interferometer to detect gravitational waves. *Journal of Instrumentation*, 7(03):P03012–P03012, mar 2012.

[16] M. Marsella et al. Virgo Reference System (VRS) Control Point Network Monographs. *Technical report, VIR-0523Y-13*, 2018.

[17] M. Beker et al. Innovations in seismic sensors driven by the search for gravitational waves. *The Leading Edge*, 35(7):590–593, 2016.

[18] Indoor data. $http://foka.ise.pw.edu.pl/virgo/NN_Data_Reparsed/$.

[19] M.G. Beker, G. Cella, R. DeSalvo, M. Doets, H. Grote, J. Harms, E. Hennes, V. Mandic, D.S. Rabeling, J.F.J. van den Brand, and C.M. van Leeuwen. Improving the sensitivity of future GW observatories in the 1 - 10Hz band: Newtonian and seismic noise. *General Relativity and Gravitation*, 43(2):623–656, 2011.

[20] M Coughlin, N Mukund, J Harms, J Driggers, R Adhikari, and S Mitra. Towards a first design of a Newtonian-noise cancellation system for Advanced LIGO. *Classical and Quantum Gravity*, 33(24):244001, 2016.